Avoidance of Convex and Concave Obstacles with Convergence ensured through Contraction

Lukas Huber[1] · Aude Billard [1] · Jean-Jacques Slotine [2]

***Abstract*—This paper presents a closed-form approach to obstacle avoidance for multiple moving convex and star-shaped concave obstacles. The method takes inspiration in harmonic-potential fields. It inherits the convergence properties of harmonic potentials. We prove impenetrability of the obstacles hull and asymptotic stability at a final goal location, using contraction theory. We validate the approach in a simulated co-worker industrial environment, with one KUKA arm engaged in a pick and place grocery task, avoiding in real-time humans moving in its vicinity and in simulation to drive wheel-chair robot in the presence of moving obstacles.**

***Index Terms*—Collision Avoidance; Optimization and Optimal Control; Autonomous Agents**

I. Introduction

ROBOTS that will work in real life environment are bound to encounter disturbances constantly, e.g. a pedestrian running in front of an autonomous car, a bird flying in front of a drone. The robot, which can not follow its initial path anymore, would have to recompute a new path within milliseconds to contour the obstacle and avoid a crash.

Control using dynamical systems (DS) is ideal to address such situations. In contrast to classical path planning, the control law is closed form, hence requires no re-planning, and can ensure impenetrability of obstacles [1], [2]. They offer stability and convergence guarantees in addition to the desired on-the-fly re-activity.

Obstacle avoidance is a classical problem in robotics and numerous approaches have been proposed [3]. Recently, powerful approaches to obstacle avoidance in cluttered environment, ensuring global path planning with global convergence properties, have been proposed, albeit at the expenses of being computationally expensive. These methods are usually evaluated offline and remain limited to quasi static environments [4].

Online (partial) replanning [5] or elastic-band methods deform locally the path and can hence be applied for dynamic environment [6]. However, as they loose global guarantees of convergence, hybrid algorithms must be used to switch between global path planning and local deformation [7]. To alleviate the computation time, recent work use customized circuitry on a chips for faster, global sampling and evaluation of all paths [8].

With improvements in hardware and computational speed, optimization algorithm such as model predictive control have become feasible for on-board use in dynamic path planning and obstacle avoidance [9]. A recent approach uses power diagrams to identify the robot's collision free, convex neighbourhood and an associated, well-known convex optimization problem generates a continuous flow [10]. This method ensures convergence for convex obstacles almost spherical curvature. In the past years, machine learning algorithms have been directly applied to sensor data, in order to infer data-driven control laws [11], but later cannot ensure impenetrability.

A common approach for obstacle avoidance are artificial potential fields [12], where each obstacle is modeled with a repulsive potential force. While each obstacle introduces topologically necessary critical points to a vector field [13], for the potential field approach they often result in (topologically unnecessary) minima [14]. Recent approaches use navigation functions which transform *star-shaped* and *trees of stars* into simpler environments where obstacles are reduced to spheres [15]. In such convex sphere worlds the problem of local minima could be mostly removed in free space and convergence to the global minima is ensured for almost all trajectories [16]. Other approaches further reduces the space to a *point-world* [17] and apply navigation function based on harmonic potentials in planar space [18].

Harmonic potential functions are particularly interesting as they guarantee that no topologically critical points arise in free space. However, as they are hard to find, potential functions are often evaluated numerically [19]. Closed-form harmonic potential functions can be generated by approximating the obstacles through linear *panels* [20]. This allows to treat concave obstacles, but is limited to static environments [1]. In other attempts, harmonic potential function are found for convex obstacles by using sliding mode between them [21]. This can be extended to linearly moving and rotating obstacles, but is limited to two dimensions [1].

We extend out previous work based on closed-form equation of harmonic potential flow around simple obstacles [22]. While the work ensures to avoid moving obstacles, it was restricted to convex obstacles. An extension to concave obstacles using discrete, sensor-based representation was offered in [23], [24], but it led to the creation of a potentially infinite number of spurious attractors on the obstacle.

This paper offers an approach to avoid multiple concave obstacles, that preserves the asymptotic stability and ensures that no more than one single trajectory leads to a spurious attractor.

Manuscript received September 11, 2018; Revised December 05, 2018; Accepted January 02, 2019. This paper was recommended for publication by editor Dezhen Song upon evaluation of the associate editor and reviewers' comments.

*This work was funded in part by the EU project Crowdbots.

[1] LASA Laboratory, Swiss Federal School of Technology in Lausanne - EPFL, Switzerland. {lukas.huber;aude.billard}@epfl.ch

[2] Nonlinear Systems Laboratory, Massachusetts Institute of Technology, USA. jjs@mit.edu

Digital Object Identifier (DOI): see top of this page.

II. Preliminaries

$\xi \in \mathbb{R}^d$ is the state of the robotic system whose dynamics is governed by an autonomous (time invariant) linear system with a single attractor ξ^a of the form:

$$\mathbf{f}(\xi) = -(\xi - \xi^a) \tag{1}$$

A. Obstacle Description

As [22], we define for each obstacle a continuous distance function $\Gamma(\xi) : \mathbb{R}^d \setminus \mathscr{X}^i \mapsto \mathbb{R}_{\geq 1}$, which allows to distinguish three regions:

$$\begin{aligned} &\text{Exterior points:} && \mathscr{X}^e = \{\xi \in \mathbb{R}^d : \Gamma(\xi) > 1\} \\ &\text{Boundary points:} && \mathscr{X}^b = \{\xi \in \mathbb{R}^d : \Gamma(\xi) = 1\} \\ &\text{Interior points:} && \mathscr{X}^i = \{\xi \in \mathbb{R}^d \setminus (\mathscr{X}^e \cup \mathscr{X}^b)\} \end{aligned} \tag{2}$$

By construction $\Gamma(\cdot)$ increases monotonically with increasing distance from the center ξ^c and has a continuous first-order partial derivative (C^1 smoothness). In this paper, we define:

$$\Gamma(\xi) = \sum_{i=1}^{d} \left(\|\xi_i - \xi_i^c\| / R(\xi)\right)^{2p} \quad \text{with} \quad p \in \mathbb{N}_+ \tag{3}$$

with $R(\xi)$ the distance from a reference point ξ^r within the obstacle to the surface ($\Gamma(\xi) = 1$) in direction $r(\xi)$ (Fig. 3a).

III. Obstacle Avoidance Algorithm

Real-time obstacle avoidance is obtained by applying a dynamic modulation matrix to the original DS given in (1):

$$\dot{\xi} = \mathbf{M}(\xi)\mathbf{f}(\xi) \qquad \text{with} \quad \mathbf{M}(\xi) = \mathbf{E}(\xi)\mathbf{D}(\xi)\mathbf{E}(\xi)^{-1} \tag{4}$$

A local modulation matrix is advantageous as it conserves existing extrema, such as a minimum in the form of an attractor and does not introduce new extrema as long as $\mathbf{M}(\cdot)$ has full rank [25]. It yields a closed form solution and the application of the matrix on the system is computationally cheap.

The modulation matrix $\mathbf{M}(\cdot)$ is composed of a basis matrix:

$$\mathbf{E}(\xi) = [\mathbf{r}(\xi)\ \ \mathbf{e}_1(\xi)\ \ ..\ \ \mathbf{e}_{d-1}(\xi)], \quad \mathbf{r}(\xi) = \frac{\xi - \xi^r}{\|\xi - \xi^r\|} \tag{5}$$

and the tangents $\mathbf{e}_{(\cdot)}(\xi)$ form a $d-1$ dimensional orthonormal basis to the gradient of the distance function $d\Gamma(\xi)/d\xi$. The reference direction $\mathbf{r}(\xi)$ is based on a reference point situated inside the obstacle (Fig. 1a). This departs from [22] and is key to avoid concave obstacles as we will see in Sec. III-C.

The associated eigenvalue matrix $\mathbf{D}(\xi)$ stretches and compresses the dynamics along the directions **e**-**r**-system. This diagonal matrix allows to modify the reference $\mathbf{r}(\xi)$ and tangent $\mathbf{e}_i(\xi)$ directions individually (Fig. 1b):

$$\mathbf{D}(\xi) = \mathbf{diag}(\lambda_r(\xi), \lambda_e(\xi), \ldots, \lambda_e(\xi)) \tag{6}$$

the eigenvalues $\lambda_{(\cdot)}(\xi)$ determine the amount of stretching in each direction.

A. Eigenvalues

As in [22], the eigenvalue associated to the first eigenvector decreases to become zero on the obstacle's hull. This cancels the flow in the direction of the obstacle and ensures that the robot does not penetrate the surface. The eigenvalues along the tangent direction increases the speed by the same magnitude in each direction. This allows the robot to move around the obstacle. Note that the eigenvalues can be set so as to ensure that the magnitude of the velocity is preserved in certain direction as required for the application. We have:

$$0 \leq \lambda_r(\xi) \leq 1 \qquad \lambda_e(\xi) \geq 1 \tag{7}$$

$$\lambda_r(\xi | \Gamma(\xi) = 1) = 0 \quad \underset{\Gamma(\xi)}{\operatorname{argmax}}\ \lambda_e(\xi) = 1 \quad \lim_{\Gamma(\xi)\to\infty} \lambda_{(\cdot)}(\xi) = 1$$

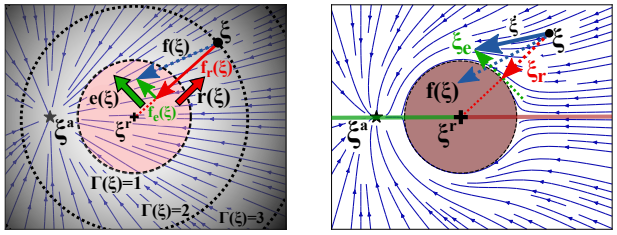

(a) Initial System **(b)** Decomposition

Fig. 1: The initial, linear system $\mathbf{f}(\xi)$ is decomposed in tangent $\mathbf{e}(\xi)$ and reference direction $\mathbf{r}(\xi)$ (a). The individual stretching along tangents and compression in reference direction allow to safely avoid the obstacle with $\dot{\xi}$ (b).

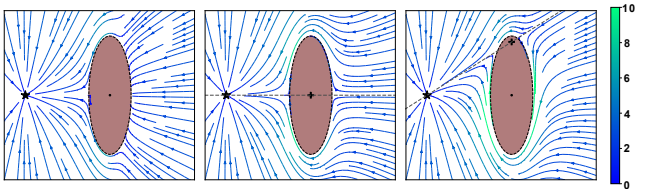

(a) No reference **(b)** Reference center **(c)** Reference top

Fig. 2: Using an orthonormal basis matrix $\mathbf{E}(\xi)$ as in [22], a local minimum might occur on the surface of the obstacle (a). The placement of the reference point $\xi^r \in \mathscr{X}^i$ marked as '+' in (b,c) guides the modulated DS around the obstacle.

Uising the existence of $\Gamma(\xi)$ see (2), that measures the distance to the obstacle's surface, we can set:

$$\lambda_r(\xi) = 1 - 1/\Gamma(\xi) \qquad \lambda_e(\xi) = 1 + 1/\Gamma(\xi) \tag{8}$$

B. Reference Point

The reference point ξ^r introduced in (5) is constraint by the fact that the basis $\mathbf{E}(\xi)$ needs to be invertible, i.e. have full rank. This is the case if the reference direction $\mathbf{r}(\xi)$ is linearly independent of the tangents $\mathbf{e}_{(\cdot)}(\xi)$ at any position. This is ensured for a reference point within a convex obstacle $\xi^r \in \mathscr{X}^i$. The reference point can be the geometric center $\xi^r = \xi^c$, but any point within the obstacle is valid (Fig. 2).

Theorem 1 *Consider an obstacle in $\mathbb{R}^d$ with boundary $\Gamma(\xi) = 1$ with respect to a reference point inside the obstacle $\xi^r \in \mathscr{X}^i$ as given in (2). Any trajectory $\{\xi\}_t$, that starts outside the obstacle, i.e. $\Gamma(\{\xi\}_0) \geq 1$ and evolves according to (4), will never penetrate the obstacle, i.e. $\Gamma(\{\xi\}_t) \geq 1, t = 0..\infty$.* **Proof:** see Appendix A.

C. Concave Obstacles

The shape of the obstacle is also constraint by the condition of $\mathbf{E}(\xi)$ having full rank from (4). Convex and concave obstacles for which there exist a reference point ξ^r inside the obstacle, from which all rays cross the boundary only once. (Fig. 3a) fulfill this condition. These obstacles are referred to as *star-shaped* and are further discussed in [15].

Many obstacles which we handle in daily life are not convex, but *star-shaped*, e.g. bottles, laptops, books. For more general concave obstacles, the hull can be extended based on a reference point ξ^r to make it *star-shaped* (Fig. 3b).

Moreover, concave obstacles can also be created by contact of several convex obstacles (Sec. IV-B).

D. Convergence to Attractor

Any smooth vector field in a sphere world has at least as many topologically critical points as obstacles [13], which are

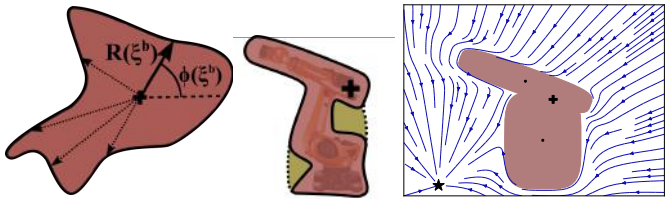

(a) Star shape **(b)** Robot hull **(c)** Flow around robot

Fig. 3: A *star-shaped* obstacle has one specific radius $R(\xi)$ in each direction $\phi(\xi)$ (a). For an obstacle, e.g. a robot arm, its hull might have to be extended (yellow) to obtain a *star-shape* (b) before evaluating the modulated DS (c). (The modulated DS is evaluated by representing the robot with two separate convex obstacles with a common reference point ξ^r.)

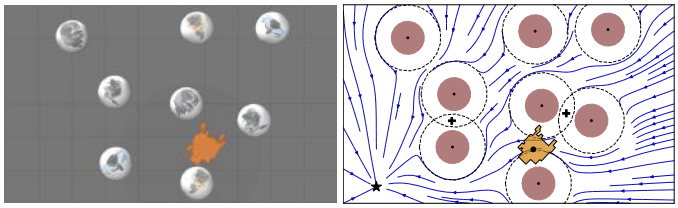

(a) Simulation wheelchair **(b)** 2D model

Fig. 4: The wheelchair (orange) tries to avoid a human crowd represented by circular obstacles (a). In order to account for the wheelchair's geometry a margin around the obstacle (dashed line) is added (b).

ideally saddle points. For a linear DS $\mathbf{f}(\xi)$ as in initial motion as in (1), there is a saddle point trajectory $\mathscr{X}^s$ behind the obstacle's reference point ξ^r (red line in Fig. 1b):

$$\mathscr{X}^s \subset \mathbb{R}^d = \{\xi \in \mathbb{R}^d : \mathbf{f}(\xi) \parallel \mathbf{r}(\xi), \|\xi - \xi^a\| > \|\xi - \xi^r\|\} \quad (9)$$

The saddle point results, because the trajectory is pointing in direction of the reference point.. Applying the decomposition with the basis matrix $\mathbf{E}(\xi)$ as given in (4) results in zero magnitude in tangent directions and therefore a straight trajectory.

Theorem 2 *Consider a time invariant, linear DS $\mathbf{f}(\xi)$ with a single attractor at ξ^a as in (1). The DS is modulated according to (4) around an obstacle with boundary $\Gamma(\xi) = 1$. Any motion $\{\xi\}_t$, $t = 0..\infty$ that starts outside the obstacle and lies not on the saddle point trajectory i.e. $\{\{\xi\}_0 \in \mathbb{R}^d \setminus \mathscr{X}^s : \Gamma(\{\xi\}_0) > 1\}$ converges to the attractor, i.e. $\{\xi\}_t \to \xi^a,\ t \to \infty$.* **Proof:** see Appendix B.

E. Leveraging Heuristics

1) Magnitude: Applying the modulation on the DS results in change of magnitude along the different basis directions (Fig. 2). While there is a decrease along the reference direction, the increase in velocity along the tangent direction is bounded to $\max(\lambda_e(\xi)) = 2$). As the basis matrix $\mathbf{E}(\xi)$ is not orthogonal, the angle $\varepsilon(\xi)$ between $\mathbf{r}(\xi)$ and the tangent plane (Fig. 9) is less than 90 degrees. Therefore, the amplitude of the DS is upper bounded by $|\xi_{max}|$:

$$|\dot{\xi}| < |\dot{\xi}_{max}| = \frac{|f(\xi)|}{\cos\varepsilon(\xi)} \max(\lambda_e(\xi)) = 2\frac{|f(\xi)|}{\cos\varepsilon(\xi)} \quad (10)$$

The maximum magnitude $|\dot{\xi}_{max}|$ occurs on the surface of the obstacle ($\Gamma(\xi) = 1$) and for an initial DS $\mathbf{f}(\xi)$ which points in a direction by $\varepsilon(\xi)$ inclined towards the normal $\mathbf{n}(\xi)$ opposite the reference direction $\mathbf{r}(\xi)$ (Fig. 2).[1]

2) Direction: In the present approach, the DS follows the border closely behind the obstacle (Fig. 2a); an alternative is to move straight towards the attractor behind and obstacle [22].

IV. Multiple Obstacles

In the presence of multiple obstacles, the nominal DS is modified by taking the weighted mean of the modulated DS $\dot{\xi}^o$ created by each obstacle $o = 1..N^o$; separately for the magnitude $\|\dot{\xi}^o\|$ and direction $\mathbf{n}^{\dot{\xi}^o}$ (Fig. 4).[2] The modulated DS for each obstacle o is given as $\dot{\xi}^o = \|\dot{\xi}\|^o \mathbf{n}^{\dot{\xi}^o}$. To balance the effect of each obstacle and to ensure that one the boundary of each obstacle the influence of the other obstacles vanish, we enforce that :

$$\sum_{k=1}^{N^o} w^o(\xi) = 1 \quad \text{and} \quad w^o(\xi \in \mathscr{X}^{b,\hat{o}}) = \begin{cases} 1 & o = \hat{o} \\ 0 & o \neq \hat{o} \end{cases} \quad (11)$$

Where N^o is the number of obstacles, and $\hat{o}$ denotes the boundary of obstacle o.

In the experiments, we set the weight w^o to be inversely proportional to the distance measure $\Gamma^o(\xi) - 1$ (notice that each obstacle can have its own distance measure Γ^o):

$$w^o(\xi) = \frac{\prod_{i \neq o}^{N^o} \left(\Gamma^i(\xi) - 1\right)}{\sum_{k=1}^{N^o} \prod_{i \neq k}^{N^o} (\Gamma^i(\xi) - 1)} \quad o = 1..N^o \quad (12)$$

The magnitude is evaluated by the weighted mean:

$$\|\dot{\xi}\| = \sum_{o=1}^{N^o} w^o \|\dot{\xi}^o\| \quad (13)$$

A. Directional interpolation

We compute the deflection from the original DS with respect to the unitary vector $\mathbf{n}^f(\xi)$, aligned with the original DS. We define the function $\kappa(\cdot) \in \mathbb{R}^{d-1}$ that projects the modulated DS from each obstacle onto a $(d-1)$-dimensional hyper-sphere with radius π (Fig. 5). [3]

$$\kappa(\dot{\xi}^o, \xi) = \arccos\left(\mathbf{n}_1^{\dot{\xi}^o}\right) \frac{\left[\hat{\mathbf{n}}_2^{\dot{\xi}^o} \ .. \ \hat{\mathbf{n}}_d^{\dot{\xi}^o}\right]^T}{\sum_{i=2}^{d} \hat{\mathbf{n}}_i^{\dot{\xi}^o}}, \quad \hat{\mathbf{n}}^{\dot{\xi}^o} = \mathbf{R}_f^T \mathbf{n}^{\dot{\xi}^o}$$

The orthonormal matrix $\mathbf{R}_f(\xi)$ is chosen such that the initial DS $\mathbf{f}(\xi)$ is aligned with the first axis $[\xi_1 \ \mathbf{0}]^T = \mathbf{R}_f(\xi)^T \mathbf{f}(\xi)$ with $\mathbf{R}_f(\xi) = \left[\mathbf{n}^f(\xi) \ \mathbf{e}_1^f(\xi) \ \ldots \ \mathbf{e}_{d-1}^f(\xi)\right]$. The vectors $\mathbf{e}_{(\cdot)}^f(\xi)$ are chosen so as to form an orthonormal basis. The weighted mean is evaluated in this κ-space (Fig. 5b):

$$\bar{\kappa}(\xi) = \sum_{o=1}^{N^o} w^o(\xi) \kappa^o(\dot{\xi}, \xi) \quad (14)$$

The direction vector of the modulated DS $\dot{\bar{\xi}}$ is then expressed back in the original space:

$$\bar{\mathbf{n}}(\xi) = \mathbf{R}_f(\xi) \left[\cos\|\bar{\kappa}(\xi)\| \quad \frac{\sin\|\bar{\kappa}(\xi)\|}{\|\bar{\kappa}(\xi)\|} \bar{\kappa}(\xi)\right]^T \quad (15)$$

With (13), the final velocity is evaluated as:

$$\dot{\bar{\xi}} = \bar{\mathbf{n}}(\xi) \|\dot{\bar{\xi}}\| \quad (16)$$

B. Intersecting Obstacles

In the case of intersecting obstacles, the above algorithm is applicable, too, but convergence only occurs if there exists one

[1] This upper bound is needed as not to exceed the hardware limit.

[2] The element-wise (of each Cartesian vector element) weighted mean of the modulated DS $\dot{\xi}^o$ for each obstacle may create stationary points.

[3] In the two-dimensional case, this hyper-sphere is a line which represents the angle between the initial DS $f(\xi)$ and the modulated DS $\dot{\xi}_k$. It has a magnitude strictly smaller than π.

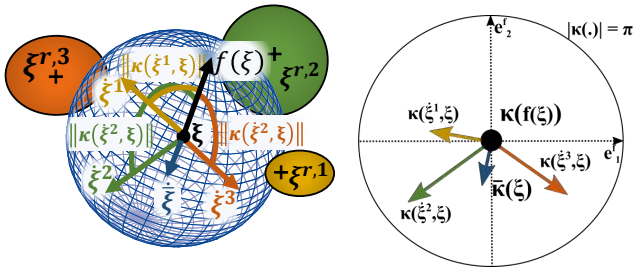

(a) Three obstacles **(b)** κ-space

Fig. 5: The velocity is evaluated separately for each of the obstacles in three-dimensional space (a). The directions are transformed to κ-space (b) where the weighted mean, $\bar{\kappa}$, is obtained.

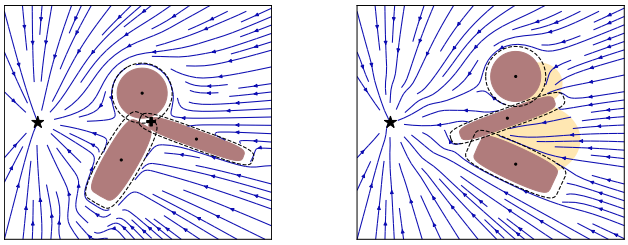

(a) Concave regions **(b)** No Common ξ^r

Fig. 6: Several intersecting convex obstacles can be avoided, if one common region exists obstacles (a). No global convergence can be observed otherwise and convergence to a local minimum (yellow) occurs (b). A *star-shape* hull can be created to exit those concave regions as in Fig. 3.

common reference point $\xi^{r,o}$ (Sec. III-B) among all obstacles. Hence, there must exist a common region. This is always the case for two intersecting obstacles. For more intersecting obstacles it happens in special cases (Fig. 6). The convex obstacles must form a *star-shape* as a group (see concave obstacle in Sec. III-C).

Furthermore, if several obstacles share one reference point ξ^r, there exists only one common, saddle point trajectory.

Theorem 3 *Consider a time invariant, linear DS* $\mathbf{f}(\xi)$ *with a single attractor at* ξ^a *as in (1). The DS is modulated according to (16) around* $N^o > 1$ *obstacles with boundaries* $\Gamma^o(\xi) = 1,\ o = 1..N^o$, *which share one common reference point* $\tilde{\xi}^r$. *Any motion* $\{\xi\}_t, t = 0..\infty$ *that starts outside the obstacles and lies not on the saddle point trajectory i.e.* $\{\{\xi\}_0 \in \mathbb{R}^d \setminus \mathscr{X}^s : \Gamma(\{\xi\}_0) > 1\}$ *converges to the attractor, i.e.* $\{\xi\}_t \to \xi^a,\ t \to \infty$. **Proof:** see Appendix C.

C. Impenetrability

On the surface of an obstacle $\hat{o}$ ($\Gamma^o(\xi \in \mathscr{X}^{b,\hat{o}}) = 1$) the corresponding weight is $w^{\hat{o}} = 1$, whereas for all other obstacles $w^o = 0,\ o \neq \hat{o}$. Therefore, the interpolation of the velocities is equal to: $\dot{\tilde{\xi}} = \dot{\xi}^o$. Impenetrability follows immediately from the impenetrability for the single obstacle in App. A.

Note that there is a singularity on the obstacles' boundary, where two surfaces intersect. This does not lead to penetration of the obstacle's boundary, since according to App. B4 no trajectory reaches the surface in finite time. Therefore, either the robot avoids this concave region and converges to the attractor, or it converges to this saddle point at the singularity, but only reaches the surface in infinite time.

D. Convergence

The magnitude (13) is by definition larger or equal to zero. Zero velocity is only obtained if the product of the weight $w^o(\xi)$ and magnitude are zero for all obstacles. This ensures that no new stationary points ($|\dot{\tilde{\xi}}| = 0$) are created.

V. Moving Obstacles

For moving obstacles the modulation is performed in the obstacle reference frame, and then transformed to the inertial frame [23]:

$$\dot{\xi} = \mathbf{M}(\xi)\left(\mathbf{f}(\xi) - \dot{\tilde{\xi}}\right) + \dot{\tilde{\xi}} \quad \text{with } \dot{\tilde{\xi}} = \dot{\xi}^{L,o} + \dot{\xi}^{R,o} \times \tilde{\xi} \quad (17)$$

with linear and angular velocity of the obstacle with respect to its center point $\dot{\xi}^{L,o}$ and $\dot{\xi}^{R,o}$, respectively and the relative position $\tilde{\xi} = \xi - \xi^c$. Avoiding moving obstacles is not a pure modulation of the DS in form of a matrix multiplication anymore, hence topographically critical points, including the attractor, can be displaced.

A. Relative Velocity

From (17), the DS on the surface a moving obstacle has a normal component which is equivalent to the obstacles velocity in this direction. As a result a robot is pulled along with a passing obstacle, e.g. a human. It might be undesired, because it creates unnecessary change of the initial DS and it might result in critical situations if the robot abruptly changes direction. This effect can be reduced by considering the obstacle's velocity in the normal direction $\mathbf{n}(\xi)$ only if it is greater than zero: $\dot{\tilde{\xi}}^o_n = \max\left(\mathbf{0}, \dot{\tilde{\xi}}^o_n\right)$.

B. Forced Attraction

The convergence to the attractor ξ^a can be enforced with a moving obstacle, by treating the region around the attractor similarly to a region around an obstacle, but with modulation matrix $M^s(\xi) = I$. The direction and magnitude of the initial DS are interpolated similarly to the case of several obstacles (Sec. IV).

The weighted sum includes the desired stationary points $(\cdot)^s$ for $s = 1..N^s$ and obstacles $(\cdot)^o$ for $o = 1..N^o$. This gives the final magnitude:

$$\|\dot{\tilde{\xi}}\| = \sum_{i=1}^{N^o} w^o_i(\xi)\|\dot{\xi}^o\| + \sum_{j=1}^{N^s} w^s_j(\xi)\|\mathbf{f}(\xi)\|, \quad \sum_i w^o_i + \sum_j w^s_j = 1$$

where the weights are chosen inverse proportional a distance measure to the corresponding feature.

C. Impenetrability

The Neumann Boundary condition from (20) is not ensured on the boundary of obstacle o, as the present obstacle avoidance method is only evaluated partially in the moving frame (Sec. V-A). While this ensures that no trajectory ever penetrates the boundary $\mathscr{X}^{b,o}$, in the specific case of obstacle avoidance, a less conservative boundary condition is sufficient: any point starting outside of the obstacle is desired to stay there at all time, but no such restriction is required for points inside the boundary as this space is never reached:

$$\left(\dot{\tilde{\xi}}^o\right)^T \cdot \mathbf{n}(\xi) \geq 0 \qquad \forall \xi \in \mathscr{X}^{b,o} \quad (18)$$

with the normal on the surface $\mathbf{n}(\xi)$ pointing away from the obstacle. The condition of (Sec V-A) ensures this inequality.

Furthermore, the forced attraction of Sec. V-B has no impact on impenetrability as long as it is done around a local

minima, because on the surface of an obstacle the weight of a stationary point is zero unless it is on the boundary of the obstacle: $w^s = 0, \text{ if } \xi^{a,s} \notin \mathscr{X}^b$. If the stationary point is on obstacle's boundary, the velocity is zero as a result of the stationary condition of the attractor and the boundary condition is verified, too.

VI. Empirical Validation

The performance of the proposed framework is evaluated on a robotic arm platform (7 DOF KUKA LWR 4+ with a 2 finger *Robotiq*-gripper). The robot is controlled at a rate of 100 Hz. The robot is simplified to a sphere shape with center at the end effector (Fig. 7b), as this is the region with the highest probability for collision. The output, the desired velocity of the end effector, is converted to joint torque using impedance controller and inverted kinematics described in [26]. The damping of the controller is chosen high enough to have the robot accurately follow the desired trajectory.
The orientation of the end-effector is kept pointing towards the ground. The robot is simplified to have a spherical geometry, with center at the end-effector. The position and orientation of moving obstacles are captured by an Optitrack system, while the geometry of the obstacles is determined manually. A safety margin of the radius of the robot model is added to each obstacle, because the obstacle avoidance method ensures impenetrability only for a point robot.

A. Scenario 1: Pick-and-place task

The first part of the empirical validation consists of a task encoded by three consecutive, linear DS, with switching occurring as soon as the end effector reaches an attractor (Fig. 7).
A) *Pick:* Objects (shopping groceries) are arriving on a conveyer belt, where the gripper is picking them up at a constant location.
B) *Place:* The objects are placed at their goal position, i.e. in a concave basket.
C) *Via-point:* To ensure a close to vertical descend onto the pick location, the robot passes by the via point.
The initial motion of three consecutive, linear DS (blue arrow in Fig. 7a) are modulated (red) to avoid the obstacles. The large obstacle (two orange ellipsoid) on the right represents the bottom and left wall of the basket. The small obstacle on the left is a *virtual*-object, the purpose of which it is to guide the motion. It but modulates the DS such that it has a small vertical motion after the picking-action (Fig. 7a), this avoids sliding along the conveyer belt. Note, that this *virtual* obstacle has the same purpose for the placing-motion as the via-point for the picking-motion, but the resulting path with using a virtual obstacle is smoother.
During the validation, the robot picks at a constant location on the conveyer belt incoming objects varying in weight and form (e.g. tea bag package at 50 grams, quick-notes packages at 300 grams). Furthermore, the position of the robot can get disturbed by applying an external force on the end effector. The robot is safely able to pick up the obstacles from the conveyer belt and place them in the basket without collision.

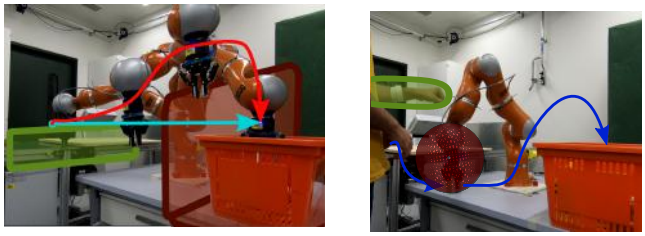

(a) Placing **(b)** Avoidance below

Fig. 7: The *pick-and-place* is a sequence of three linear DS (blue arrow) which are modulated to avoid the obstacles to obtain the final DS (red arrow) in (a). The robot path is adapted in real-time in presence of new obstacles (b). The model of the robot is simplified to be spherical around the end effector (red sphere).

The disturbance leads to a change in path but has no effect on the success of the execution.

B. Scenario 2: human interference in robot task

In the second scenario, a human is interacting with the robot, as the human is helping the robot on the conveyer belt during the packing task (e.g. handling complicate or delicate obstacles). The robot has full knowledge of the position of the human forearms. Due to the slow motion of the arms and the high update rate, they are simplified to be quasi static.
The forearms are modeled as ellipsoids with a large hull to account for the dimensions of the end effector. The forearms can intersect with the other obstacles or each other and create concave forms as they move freely in space. The base task is the same pick-and-place task as in Scenario 1.
The present method is able to find a safe path to execute the pick-and-place task in real-time. However, the trajectory vary greatly depending on the newly introduced obstacle (the forearm). The algorithm is also able to avoid the concave region which is created, if the two obstacles representing the arms intersect.

VII. Discussion and Future Work

The algorithm depends on choosing well the reference point inside the obstacle, as this shapes the modulation. We set conditions on the set of feasible reference points but left it to practitioners to decide which is most suitable for their application. The choice of this reference point can become challenging if the modulation matrix must vary in time.

A. Models of the Robot and the World

The algorithm was evaluated with prior full knowledge of the obstacle form, and the position and velocity estimate is assumed being error free. Future work should investigate the effect on uncertainties in the robot's state as well as the robot surface being learned based on sensor data.
All control inputs and proofs are based on the assumption of a point-shaped, zero-mass robot. While the obstacle hull can be expanded to account for the robots dimensions, this introduces constraint on the movement of the robot as well as the positions of the obstacle. Furthermore, the velocity based controller does not take into account the inertia of the robot. This might lead to collision in confined spaces and at higher speeds, the controller needs to be extended to includes the robot's dynamics for the application.

B. Restrictions on Dynamical Systems and Obstacles

The present algorithm needs all obstacles in *star-shape*, for this modification of the robot hull might be required. *Star-shapes* include any form created by two convex, intersecting obstacles, as well as being able to model complex obstacles relatively close. On the other hand, the algorithm cannot model a human or even an arm-robot itself closely, as the high number of limbs and configuration most the time exceeds the properties of being *star-shaped*. Hence, an extension of the algorithm to more general concave obstacles is desired.
In this report, we focused on input DS which has a linear form. While this is a good choice for finding a direct path to a goal position in the presence of obstacles, in many task may require more complex input systems, e.g. polishing or painting of surface. Future work should extend the present algorithm to nonlinear DS. (This might be an algorithm not based on a matrix modulation.)

C. Optimal Path

The obstacle avoidance happens in a two dimensional, linear plane, no matter the number of dimensions of the space (Sec. B). This is often not the optimal case, e.g. for the case of a long ellipsoid (such as a forearm), where the modulation around the longest axis is equally likely as around the shorter ones. The present algorithm should extended to optimize the path by leveraging heuristics based on different cost metrics (e.g. shortest path, least acceleration).
Furthermore, the combination of the present method with global path planning such as RRT should be explored, similar to [5], [7].

VIII. Conclusion

While there certainly exist faster algorithms, or ones which can handle more complex spaces; the present method is a simple and fast, closed-form method, which is able to avoid relatively complex environments while still ensuring convergence. Furthermore, it is general enough to be applied to platforms with different sensors, movement and dimensions. Hence it has a large range of applications, ranging from robot arms along conveyer belts, which could work interactively with humans, but also autonomous vehicles which continue the desired motion rather than stop in the presence of obstacles, such as autonomous wheel chairs in highly populated areas.

Appendix

A. Proof of Theorem 1

The initial DS can be written as a linear combination of two vectors: one contained in the tangent hyper-plane $\mathbf{f}_e(\xi)$ and the other parallel to the reference direction $\mathbf{f}_r(\xi) \parallel \mathbf{r}(\xi)$:

$$\mathbf{f}(\xi) = \mathbf{f}_r(\xi) + \mathbf{f}_e(\xi) = \|\mathbf{f}_r(\xi)\|\mathbf{r}(\xi) + \|\mathbf{f}_e(\xi)\|\mathbf{e}(\xi) \quad (19)$$

where $\mathbf{e}(\xi)$ is a linear combination of all tangent vectors $\mathbf{e}_i(\xi)$, $i = 1..d-1$, which are described in (5).
For any point on the boundary ($\Gamma(\xi) = 1$) the modulated DS follows from (4) and the condition in (8):

$$\dot{\xi} = \lambda_r(\xi)\mathbf{f}_r(\xi) + \lambda_t(\xi)\mathbf{f}_e(\xi) = \lambda_t(\xi)\|\mathbf{f}_e(\xi)\|\mathbf{e}(\xi) \quad \forall\, \xi \in \mathscr{X}^b$$

According to the *von Neuman* boundary condition, impenetrability is ensured if there is no velocity in normal direction on the surface of the obstacle:

$$\mathbf{n}(\xi)^T\, \dot{\xi} = \mathbf{n}(\xi)^T \mathbf{e}(\xi)\|\dot{\xi}\| = 0 \quad \forall\, \xi \in \mathscr{X}^b \quad (20)$$

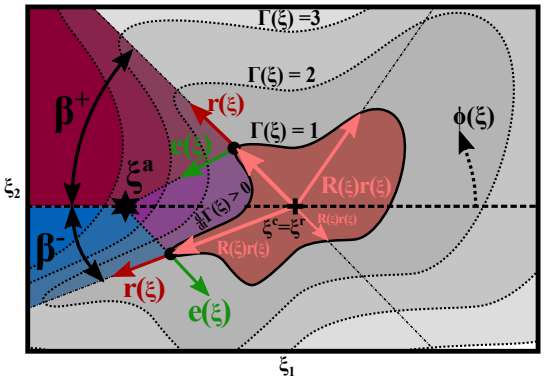

Fig. 8: Any trajectory starting outside the obstacle in the positive or negative half-plane ends up in the invariant cone-region, purple or red, respectively.

since per definition the tangent hyper-plane is orthogonal to $\mathbf{n}(\xi) = d\Gamma(\xi)/d\xi$. ■

B. Proof of Theorem 2

The proof of the algorithm of Sec. II consists of four steps:
1. Reduction of d-dimensional problem to 2D (Sec. B1)
2. Proof of existence of cone-shaped invariant sets including the attractor (blue and red cone in Fig. 8 (Sec. B2 & B3)
3. Proof that all trajectories except the saddle point line reach this invariant set (Sec. B3 and Sec. B4)
4. Proof of convergence to the attractor through contraction in this invariant set (Sec. B5)

1) Reduction to two dimensional problem: Let us consider a linear, two dimensional plane spanned by the current position ξ, the attractor ξ^a and the reference point inside the obstacle ξ^r. By definition, the reference direction $\mathbf{r}(\xi)$ from (5) and the initial DS $\mathbf{f}(\xi)$ from (1) are also contained in the linear, 2-dimensional reference plane plane $\mathscr{S}^r(\xi)$:

$$\{\xi,\, \xi^a,\, \xi^r\} \in \mathscr{S}^r(\xi) \quad \Rightarrow \quad \mathbf{r}(\xi),\, \mathbf{f}(\xi) \in \mathscr{S}^r(\xi) \quad (21)$$

Using (19) we can write:

$$\dot{\xi} = \mathbf{M}(\xi)\mathbf{f}(\xi) = \lambda_r(\xi)\mathbf{f}_r(\xi) + \lambda_e(\xi)\mathbf{f}_e(\xi) \quad (22)$$

Hence, the following can be concluded:

$$\mathbf{f}_r(\xi) \in \mathscr{S}^r(\xi) \Rightarrow \mathbf{f}_e(\xi) \in \mathscr{S}^r(\xi) \Rightarrow \dot{\xi} \in \mathscr{S}^r(\xi) \quad (23)$$

In other words, the modulated DS is parallel to the two dimensional, linear hyper-plane. Hence, any motion starting in linear, two dimensional hyper-plane $\{\xi\}_0 \in \mathscr{S}(\{\xi\}_0)$, remains in this hyper-plane for all times, i.e. $\{\xi\}_t \in \mathscr{S}(\{\xi\}_0)\ t = 0..\infty$. Further proofs of convergence can be conducted in two dimensions, and is applicable to the d-dimensional case. Without loss of generality, for further proof the attractor is placed at the origin $\xi^a = \mathbf{0}$ and the reference point of the obstacle is $\xi^r = [d_1\ \ 0]$, with $d_1 > 0$ (Fig. 8).

2) Region with Movement Away from the Obstacle: We want to show that there exists a region, where the DS is moving away from the obstacle, i.e. $d\Gamma(\xi)\ dt > 0$. Close to the obstacle with $\Gamma(\xi) - 1 << 1$, following equality for any level function $\Gamma(\xi)$ given in (2) holds $\Gamma(\xi)R(\xi)\mathbf{r} = \xi - \xi^r$, with $R(\xi) \in \mathbb{R}_{\geq 0}$ the distance to the center to the surface of the obstacle in reference direction (Fig. 8). We define $\tilde{\mathbf{E}}(\xi) = [R(\xi)\mathbf{r}\ \ \mathbf{e}]$ where $\mathbf{e}(\xi)$ from (5) is perpendicular to $d\Gamma(\xi)/d\xi$, to express the change of the level function close

to the surface:

$$\begin{aligned}\begin{bmatrix}\frac{d\Gamma}{dt} & 0\end{bmatrix}^T &= \frac{d}{dt}\left(\tilde{\mathbf{E}}(\xi)^{-1}(\xi-\xi^r)\right)\\ &= -\tilde{\mathbf{E}}(\xi)^{-1}\frac{d}{dt}\tilde{\mathbf{E}}(\xi)\tilde{\mathbf{E}}(\xi)^{-1}(\xi-\xi^r)+\tilde{\mathbf{E}}(\xi)^{-1}\mathbf{M}(\xi)\xi\\ &= -\begin{bmatrix}0 & (\cdot)\\ (\cdot) & (\cdot)\end{bmatrix}\begin{bmatrix}(\cdot)\\ 0\end{bmatrix} - \mathbf{diag}\left(1/R,\,1\right)\mathbf{D}\,\mathbf{E}^{-1}\xi\end{aligned}$$

The first diagonal element of $\tilde{\mathbf{E}}(\xi)^{-1}\frac{d}{dt}\tilde{\mathbf{E}}(\xi)$ is zero, because the derivative of the first row, the vector to the surface, is parallel to the tangent, i.e. $\frac{d}{dt}R(\xi)\mathbf{r}(\xi) \parallel \mathbf{e}(\xi)$. Furthermore, the second element of $\tilde{\mathbf{E}}(\xi)^{-1}(\xi-\xi^r)$ is zero, since $\xi-\xi^r \parallel \mathbf{r}(\xi)$. If the position of the robot expressed in **r**-**e**-basis is negative: $\left(\mathbf{E}^{-1}\xi\right)_r = \xi_r < 0 \;\Rightarrow\; \frac{d}{dt}\Gamma(\xi) = -R(\xi)\lambda_r(\xi)\xi_r > 0$, and the DS moves away from the obstacle (purple triangle region in Fig. 8). This is intuitively, the region where the initial DS is already moving away from the robot: $\mathbf{f}(\xi)^T\cdot\frac{d}{d\xi}\Gamma(\xi) < 0$.

3) Convergence to Cone Region: In order for any trajectory expect for the saddle point trajectory $\mathscr{X}^S$ given in (9) to converge to the cone region, the reference angle $\phi(\xi) = \arctan\left(\xi_2/(\xi_1-d_1)\right)$ must decrease, where $d_1 > 0$ corresponds to the position of the reference point on the ξ_1-axis. This time derivative is evaluated with (4) as:

$$\dot{\phi}(\xi) = \tilde{\xi}\times\mathbf{f}(\xi)/\|\tilde{\xi}\|^2 = \lambda_e(\xi)d_1\xi_2/\|\tilde{\xi}\|^2 \tag{24}$$

and $\tilde{\xi} = \xi - [d_1\;\;0]$. As the eigenvalue $\lambda_e(\xi)$ is larger than zero, (24) is positive for $\xi_2 > 0$, and negative on the other half plane. This leads to two deductions. Firstly, any point starting outside the obstacle and not on the saddle point, reaches a cone region with $|\pi-\phi(\xi)| \le \beta \le \min(\beta^+,\beta^-)$ with $\beta > 0$. Secondly, any cone region outside the obstacle which contains the attractor ξ^a and has its center at ξ^r is invariant.

4) Staying Outside the Obstacle for Finite Time: While any trajectory ends up within the cone-boundary in finite time, the invariant set is only strictly outside the obstacle $\xi \in \mathscr{X}^e$. We therefore want to show that the robot stays outside the obstacle for finite time.

Components in direction of the $\mathbf{n}(\xi) = d\Gamma/d\xi$ are referred to as $(\cdot)_n$. Moreover, the velocity is bounded in a real system, with the maximum velocity in normal direction v_n. The time to transit between arbitrary levels Γ_0 and Γ_1 can be evaluated with (7) as:

$$\begin{aligned}t^b(\xi) &= \int_{\Gamma_0}^{\Gamma_1}\frac{d\Gamma}{\dot{\xi}_n} = \int_{\Gamma_0}^{\Gamma_1}\frac{d\Gamma}{\lambda_r(\xi)f_n(\xi)} = \int_{\Gamma_0}^{\Gamma_1}\frac{1}{f_n(\xi)}\frac{\Gamma}{\Gamma-1}\,d\Gamma\\ &\ge \frac{1}{v_n}\left[\Gamma_0+\log(\Gamma_0-1)-\Gamma_1-\log(\Gamma_1-1)\right]\end{aligned} \tag{25}$$

Starting outside the obstacle $\Gamma_0 > 1$, and having the goal on the surface $\Gamma_1 = 1$, the time results as: $\lim_{\Gamma_1\to 1} t^b(\xi) \to \infty$. From this it follows, that any point starting outside the obstacle does not reach the surface in finite time.

5) Contraction Analysis: The modulated dynamical system from (4) restated as a function of $\mathbf{g}(\cdot)$:

$$\dot{\xi} = \mathbf{g}(\xi,\xi) = \mathbf{M}(\xi)\mathbf{f}(\xi) = \mathbf{M}(\xi)\xi \tag{26}$$

Using Partial Contraction Theory [27], the virtual system is chosen to as a function of the new variable $\gamma \in \mathbb{R}^d$:

$$\dot{\gamma} = \mathbf{g}(\gamma,\xi) = -\mathbf{M}(\xi)\gamma \tag{27}$$

If the system $\mathbf{g}(\cdot)$ is contracting with respect to γ, and it has the two particular solutions $\gamma = \xi$ and $\gamma = \xi^a = \mathbf{0}$. It follows from [27] that the ξ-system exponentially tends to $\xi^a = \mathbf{0}$. Hence, we need to show that the system is contracting [28] with respect to γ. A possible contraction metric is $\mathbf{P}(\xi) = \Theta(\xi)^T\Theta(\xi)$ with:

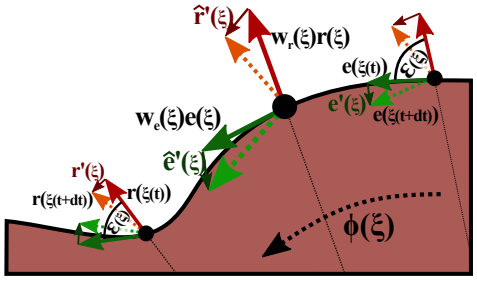

Fig. 9: The derivative of the basis matrix $\mathbf{E}(\xi)$ and the partial transformation $\hat{\mathbf{E}}(\xi)$ for $\xi_2 > 0$.

$$\Theta(\xi) = \hat{\mathbf{E}}(\xi)^{-1} = \begin{bmatrix}w_r(\xi)\mathbf{r}(\xi) & w_e(\xi)\mathbf{e}(\xi)\end{bmatrix}^{-1} \tag{28}$$

where $\Theta(\xi)$ is a uniformly invertible square matrix based on (5). The system is contracting with respect to the metric $\mathbf{P}(\xi)$, if the symmetric part of the generalized Jacobian $\mathbf{F}_{sym} = \mathbf{F} + \mathbf{F}^T$ is negative definite with:

$$\begin{aligned}\mathbf{F} &= \frac{d}{dt}\Theta\,\Theta^{-1} + \Theta\frac{\partial\mathbf{g}(\gamma,\xi)}{\partial\gamma}\Theta^{-1}\\ &= -\hat{\mathbf{E}}^{-1}(\xi)\frac{d}{dt}\hat{\mathbf{E}}(\xi) - \hat{\mathbf{E}}(\xi)^{-1}\mathbf{E}(\xi)\mathbf{D}(\xi)\mathbf{E}(\xi)^{-1}\hat{\mathbf{E}}(\xi)\end{aligned} \tag{29}$$

where $\hat{\mathbf{E}}(\xi)^{-1}\mathbf{E}(\xi) = \mathbf{diag}\left(w_r(\xi),\,w_e(\xi)\right)$. Hence the second therm is $-\mathbf{diag}(\lambda_r(\xi),\,\lambda_e(\xi))$. The rows of the first therm $\dot{\mathbf{r}}$ and $\dot{\mathbf{e}}$ are evaluated as:

$$\begin{aligned}\hat{\mathbf{E}}^{-1}\frac{d}{dt}\hat{\mathbf{E}} &= \hat{\mathbf{E}}^{-1}\begin{bmatrix}\dot{w}_r\mathbf{r}+w_r\frac{d}{dt}\mathbf{r} & \dot{w}_e\mathbf{e}+w_e\frac{d}{dt}\mathbf{e}\end{bmatrix}\\ &= \begin{bmatrix}\frac{\dot{w}_r}{w_r} - \|\dot{\mathbf{r}}\|\frac{1}{\tan\varepsilon} & \frac{w_e}{w_r}\|\dot{\mathbf{r}}\|\mathrm{sign}(\mathbf{e}^T\cdot\dot{\mathbf{r}})\frac{1}{\sin\varepsilon}\\ \frac{w_r}{w_e}\|\dot{\mathbf{e}}\|\mathrm{sign}(\mathbf{r}^T\cdot\dot{\mathbf{e}})\frac{1}{\sin\varepsilon} & \frac{\dot{w}_e}{w_e} - \|\dot{\mathbf{e}}\|\frac{1}{\tan\varepsilon}\end{bmatrix}\end{aligned} \tag{30}$$

with $\cos\varepsilon(\xi) = \mathbf{r}(\xi)^T\cdot\mathbf{e}(\xi)$, $\dot{\mathbf{r}} = \frac{d}{dt}\mathbf{r}(\xi)$, and $\dot{\mathbf{e}} = \frac{d}{dt}\mathbf{e}(\xi)$ as can be seen in Fig. 9. Furthermore, under the condition that $\hat{\mathbf{E}}(\xi)$ has full rank (Sec. III-B) we have $\varepsilon \in]0,\pi[$.

Negative definiteness is verified if and only if the determinant of the symmetric part of the generalized Jacobian is positive definite:

$$\begin{aligned}\det\left(\mathbf{F}_{sym}\right) &= \left(\frac{\dot{w}_r}{w_r} - \frac{\|\dot{\mathbf{r}}\|}{\tan\varepsilon} + \lambda_r\right)\left(\frac{\dot{w}_e}{w_e} - \frac{\|\dot{\mathbf{e}}\|}{\tan\varepsilon} + \lambda_e\right)\\ &\quad - \frac{1}{4\sin^2\varepsilon}\left(\frac{w_e}{w_r}\|\dot{\mathbf{r}}\|\mathrm{sign}(\mathbf{e}^T\cdot\dot{\mathbf{r}}) + \frac{w_r}{w_e}\|\dot{\mathbf{e}}\|\mathrm{sign}(\mathbf{r}^T\cdot\dot{\mathbf{e}})\right)^2 > 0\end{aligned} \tag{31}$$

and its trace is negative definite:

$$\mathrm{tra}\left(\mathbf{F}_{sym}\right) = -\left(\frac{\dot{w}_r}{w_r} - \frac{\|\dot{\mathbf{r}}\|}{\tan\varepsilon} + \lambda_r\right) - \left(\frac{\dot{w}_e}{w_e} - \frac{\|\dot{\mathbf{e}}\|}{\tan\varepsilon} + \lambda_e\right) < 0$$

where $(\cdot)_r$ and $(\cdot)_e$ refer to the direction $\mathbf{r}(\xi)$ and $\mathbf{e}(\xi)$, respectively. We define the partial derivative with respect to ϕ as $(\cdot)' = \partial(\cdot)/\partial\phi$. One has $\|\mathbf{r}'\| = 1$ and $\mathrm{sign}(\mathbf{e}^T\cdot\mathbf{r}') = 1$ (Fig. 9). Conversely, the dot product $(\mathbf{r}^T\cdot\mathbf{e}')$ is positive only in a strictly concave region. Moreover, from (8) we have $\lambda_r(\xi) \ge 0$ and $\lambda_e(\xi) \ge 1$. For $\xi_2 > 0$, we rewrite the above inequalities:

$$w_r'(\phi) > w_r/\tan\varepsilon \qquad w_e'(\phi) > w_e\left(\|\mathbf{e}'\|/\tan\varepsilon - 1/\dot{\phi}\right)$$

$$\left(\frac{w_r'}{w_r} - \frac{1}{\tan\varepsilon}\right)\left(\frac{w_e'}{w_e} - \frac{\|\mathbf{e}'\|}{\tan\varepsilon} + \frac{1}{\dot{\phi}}\right) > \frac{\left(\frac{w_e}{w_r} + \frac{w_r}{w_e}\|\mathbf{e}'\|\mathrm{sign}(\mathbf{r}^T\mathbf{e}')\right)^2}{4\sin^2\varepsilon}$$

and analogously for the negative half-plane. These three conditions put lower limits on $w_r'(\phi)$ and $w_e'(\phi)$.

There can be found w_r and w_e which fulfill the conditions, i.e.

$$w_r(\phi) = w_e(\phi) = \exp\left(\left(\frac{\|\mathbf{e}'\|_{max}}{\tan(\varepsilon_{min})} + C\right)|\phi|\right) \tag{32}$$

with $C > \frac{1+\|\mathbf{e}'\|_{max}}{2\|\sin\varepsilon\|_{min}}$.
Note that $\sin\varepsilon$ and $\tan\varepsilon$ are never equal zero, they might be very small, and thus w'_r and w'_e might be large. However, this does not contradict the existence of a contraction metric or the contraction of the system. ■

C. Proof of Theorem 3

The modulation of the initial DS described in Sec. IV, can be expressed as a linear combination of the each individual modulation $\dot{\tilde{\xi}}^o$ for $o = 1..N^o$ and the initial DS $\mathbf{f}(\xi)$:

$$\dot{\tilde{\xi}} = h^0(\xi)\mathbf{f}(\xi) + \sum_{o=1}^{N^o} h^o(\xi)\mathbf{M}^o(\xi)\xi \tag{33}$$

where $h^i(\xi) \geq 0, \;\; i = 0..N^o$ are (unknown) scalar weights. The group of obstacles share one common reference point $\tilde{\xi}^r = \xi^{r,o}$. Hence, the reduction of the d-dimensional system to two dimension from Appendix B1 can be applied. The coordinate system with $\xi = [\xi_1 \;\; \xi_2]^T$ is the same for all obstacles (Fig. 9). Equation (24) can be restated for all the individually, modulated DS by each of the N^o obstacles:

$$\dot{\phi}^o(\xi) \cdot \text{sign}(\xi_2) \geq 0 \quad \xi \in \mathscr{X}^{e,o},\, \xi_2 \neq 0 \;\; \forall\, o \in 1..N^o \tag{34}$$

and a similar condition for the initial DS $\mathbf{r}(\xi) \times \mathbf{f}(\xi)\,\text{sign}(\xi_2) > 0$. It follows that the DS converges to the line with $\phi = \pi$ behind the obstacles, since the angle is always increasing.
Furthermore, there can be found two half-cone regions with $\phi \in]\beta^+, \pi]$ and $\phi \in]-\pi, \beta^-]$ with $\beta^+ > 0$ and $\beta^- < 0$ respectively (Fig. 9), where the modulation of object $\hat{o}$ dominates. Such that the final DS from (33) can be rewritten as a reduced weighted sum: $\dot{\tilde{\xi}} = \hat{h}^0(\xi)\mathbf{f}(\xi) + \hat{h}^{\hat{o}}(\xi)\mathbf{M}^{\hat{o}}(\xi)\dot{\xi}$. Both weights $\hat{h}^0(\xi) \geq 0$ and $\hat{h}^{\hat{o}}(\xi) \geq 0$ are unknown. There might be different dominant obstacles $\hat{o}$ for the positive and negative cones (blue and purple in Fig. 9). The generalized Jacobian is evaluated similarly to (29) as:

$$\mathbf{F} = \hat{\mathbf{E}}^{-1}(\xi)\frac{d}{dt}\hat{\mathbf{E}}(\xi) - \left(\hat{h}^{\hat{o}}\mathbf{D} + \hat{h}^0(\xi)\mathbf{I}\right) \tag{35}$$

where the metric $\hat{\mathbf{P}}(\xi) = (\hat{\mathbf{E}}^{-1})^T\hat{\mathbf{E}}^{-1}$ is based on the obstacle $\hat{o}$. Since the condition in (32) are chosen conservatively, the system is partially contracting using the same constraints for the weights, hence the same contraction metric. It follows that the system is exponentially converging in the presence of multiple obstacles with one common reference point. ■

REFERENCES

[1] H. J. S. Feder and J.-J. Slotine, Real-time path planning using harmonic potentials in dynamic environments, in Robotics and Automation, 1997. Proceedings., 1997 IEEE International Conference on, IEEE, vol. 1, 1997, pp. 874881.

[2] S. M. Khansari-Zadeh and A. Billard, Learning stable nonlinear dynamical systems with gaussian mixture models, IEEE Transactions on Robotics, vol. 27, no. 5, pp. 943957, 2011.

[3] H. M. Choset, S. Hutchinson, K. M. Lynch, G. Kantor, W. Burgard, L. E. Kavraki, and S. Thrun, Principles of robot motion: theory, algorithms, and implementation. MIT press, 2005.

[4] S. M. LaValle and J. J. Kuffner Jr, Rapidly-exploring random trees: Progress and prospects, 2000.

[5] O. Brock and O. Khatib, Elastic strips: A framework for motion generation in human environments, The International Journal of Robotics Research, vol. 21, no. 12, pp. 10311052, 2002.

[6] D. Ferguson, N. Kalra, and A. Stentz, Replanning with rrts, in Robotics and Automation, 2006. ICRA 2006. Proceedings 2006 IEEE International Conference on, IEEE, 2006, pp. 12431248.

[7] J. Vannoy and J. Xiao, Real-time adaptive motion planning (ramp) of mobile manipulators in dynamic environments with unforeseen changes, IEEE Transactions on Robotics, vol. 24, no. 5, pp. 11991212, 2008.

[8] S. Murray, W. Floyd-Jones, Y. Qi, D. J. Sorin, and G. Konidaris, Robot motion planning on a chip., in Robotics: Science and Systems, 2016.

[9] J. Ji, A. Khajepour, W. W. Melek, and Y. Huang, Path planning and tracking for vehicle collision avoidance based on model predic-tive control with multiconstraints,IEEE Transactions on Vehicular Technology, vol. 66, no. 2, pp. 952964, 2017.

[10] O. Arslan and D. E. Koditschek, Exact robot navigation using power diagrams, in Robotics and Automation (ICRA), 2016 IEEE International Conference on, IEEE, 2016, pp. 18.

[11] J. Michels, A. Saxena, and A. Y. Ng, High speed obstacle avoidance using monocular vision and reinforcement learning, in Proceedings of the 22nd international conference on Machine learning, ACM, 2005, pp. 593600.

[12] O. Khatib, Real-time obstacle avoidance for manipulators and mobile robots, The international journal of robotics research, vol. 5, no. 1, pp. 9098, 1986.

[13] D. E. Koditschek and E. Rimon, Robot navigation functions on manifolds with boundary, Advances in applied mathematics, vol. 11, no. 4, pp. 412442, 1990.

[14] E. Rimon and D. E. Koditschek, The construction of analytic diffeomorphisms for exact robot navigation on star worlds, Transactions of the American Mathematical Society, vol. 327, no. 1, pp. 71116, 1991.

[15] E. Rimon and D. E. Koditschek, Exact robot navigation using artificial potential functions, IEEE Transactions on robotics and automation, vol. 8, no. 5, pp. 501518, 1992

[16] S. Paternain, D. E. Koditschek, and A. Ribeiro, Navigation functions for convex potentials in a space with convex obstacles, IEEE Transactions on Automatic Control, 2017.

[17] S. G. Loizou, The navigation transformation, IEEE Transactions on Robotics, vol. 33, no. 6, pp. 15161523, 2017.

[18] S. G. Loizou, Closed form navigation functions based on harmonic potentials, in Decision and Control and European Control Conference(CDC-ECC), 2011 50th IEEE Conference on, IEEE, 2011, pp. 63616366.

[19] C. I. Connolly, J. B. Burns, and R. Weiss, Path planning using laplaces equation, in Robotics and Automation, 1990. Proceedings., 1990 IEEE International Conference on, IEEE, 1990, pp. 21022106.

[20] J.-O. Kim and P. K. Khosla, Real-time obstacle avoidance using harmonic potential functions, IEEE Transactions on Robotics and Automation, vol. 8, no. 3, pp. 338349, 1992.

[21] J. Guldner and V. I. Utkin, Sliding mode control for an obstacle avoidance strategy based on an harmonic potential field, in Decision and Control, 1993., Proceedings of the 32nd IEEE Conference on, IEEE, 1993, pp. 424429.

[22] S. M. Khansari-Zadeh and A. Billard, A dynamical system approach to realtime obstacle avoidance, Autonomous Robots, vol. 32, no. 4, pp. 433454, 2012.

[23] S. Khansari-Zadeh, A dynamical system-based approach to modeling stable robot control policies via imitation learning, PhD Thesis, 2012.

[24] M. Saveriano and D. Lee, Distance based dynamical system modulation for reactive avoidance of moving obstacles, in Robotics and Automation (ICRA), 2014 IEEE International Conference on, IEEE, 2014, pp. 56185623.

[25] K. Kronander, M. Khansari, and A. Billard, Incremental motion learning with locally modulated dynamical systems, Robotics and Autonomous Systems, vol. 70, pp. 5262, 2015.

[26] K. Kronander and A. Billard, Passive interaction control with dynamical systems, IEEE Robotics and Automation Letters, vol. 1, no. 1, pp. 106113, 2016.

[27] W. Wang and J.-J. E. Slotine, On partial contraction analysis for coupled nonlinear oscillators, Biological cybernetics, vol. 92, no. 1, pp. 3853, 2005.

[28] W. Lohmiller and J.-J. E. Slotine, On contraction analysis for nonlinear systems, Automatica, vol. 34, no. 6, pp. 683696, 1998.